

Document downloaded from:

<http://hdl.handle.net/10251/182393>

This paper must be cited as:

Pachano, L.; Xu, C.; García-Oliver, JM.; Pastor Enguádanos, JM.; Novella Rosa, R.; Kundu, P. (2021). A two-equation soot-in-flamelet modeling approach applied under Spray A conditions. *Combustion and Flame*. 231:1-11.
<https://doi.org/10.1016/j.combustflame.2021.111488>



The final publication is available at

<https://doi.org/10.1016/j.combustflame.2021.111488>

Copyright Elsevier

Additional Information

A two-equation soot-in-flamelet modeling approach applied under Spray A conditions

Author names and affiliations

Leonardo Pachano^{a,1}, Chao Xu^b, Jose M. García-Oliver^a, Jose M. Pastor^a, Ricardo Novella^a, Prithwish Kundu^b

^a CMT-Motores Térmicos – Universitat Politècnica de València, Camino de Vera s/n, 46022 Valencia, Spain

^b Energy Systems Division, Argonne National Laboratory, Lemont, IL 60439, USA

Corresponding author

Jose M. García-Oliver

E-mail address: jgarciao@mot.upv.es

Full-length Article

Abstract

Soot production (including formation and oxidation) is studied in the transient, high-pressure and turbulent *n*-dodecane Spray A flames from the Engine Combustion Network (ECN) using computational fluid dynamics (CFD) simulations. A two-equation soot-in-flamelet modeling approach is applied within the framework of the Unsteady Flamelet Progress Variable (UFPV) model and results are validated against experimental data. Equations for soot mass fraction and soot number density derived in the mixture fraction space are solved in the context of detailed flamelet calculations. Source terms for the different steps in the soot chemistry are tabulated and incorporated in the flamelet manifold. For the reference condition, the modeling approach based on the tabulated flamelet manifold reduces the computational cost of a CFD calculation by approximately 40 times compared to a non-tabulated well-mixed (WM) modeling approach. The soot-in-flamelet approach is then extended to study the effect of ambient oxygen concentration, ambient mixture composition and ambient temperature on soot production.

¹ Present address: IFP Energies Nouvelles, 1-4 avenue de Bois-Préau, 92852 Rueil-Malmaison, France

Results show that the modeling approach is able to capture the experimental trends for the soot volume fraction (SVF) with good quantitative agreement, especially in the soot ramp-up region.

Keywords

Soot modeling, flamelet, turbulent spray, chemistry tabulation

1 Introduction

Despite recent initiatives to gradually ban the use of internal combustion engines (ICEs), there are solid arguments pointing out to diversity as the key for the future in the transportation sector in which the development of ICEs is still much needed [1,2]. The ICE is the most suitable technology for many applications that demand functionality in a wide range of regimes and loads. Such is the case of heavy-duty applications in which the ICE is the primary choice. The high-energy density of fuels used in ICEs is the essence of its suitability in contrast to battery-based systems. For instance, the energy density in a lithium-ion battery is approximately two orders of magnitude lower than that of gasoline [3]. Unquestionably, the highly suitable ICE has its own share of challenges to be addressed. In compression ignition (CI) engines, the most relevant type of ICEs for the present work, flexibility and fuel efficiency come at the expense of the trade-off between NO_x and soot emissions. In particular, soot has attracted increased attention over the past years as it poses a threat on the environment and human health. On one hand, soot has been reported to contribute to the change in global surface air temperature as part of carbonaceous aerosols in the atmosphere [4–6] or by deposition on snow [7,8]. On the other hand, the inhalation of soot particles may cause cardiopulmonary diseases [9–12]. In response, stricter legislation on particle matter emissions has been introduced. In Europe, for example, the allowed particle emission for Diesel passenger cars dropped from $1.4 \times 10^{-4} \text{ kg/km}$ in the early 90's to $0.045 \times 10^{-4} \text{ kg/km}$ and $6 \times 10^{11} \text{ particles/km}$ with the current legislation [13].

Combustion in a CI engine is naturally a highly complex, multi-physical process. Thus, the study of idealized configurations which yet possess rich physics is a more approachable path to understanding fundamental phenomena in CI engines. One representative configuration is the optically accessible, high-temperature, high-pressure vessel [14,15] which allows using single-hole nozzle spray experiments to study a range of engine-relevant phenomena. Many institutions around the world have come together within the Engine Combustion Network (ECN) by performing experiments at engine-relevant conditions. As a result, a rich

experimental database is available [16] thus enabling model validation for predictive computational fluid dynamics (CFD) simulations. Among different conditions available in the ECN, Spray A is a well-documented experiment in which liquid *n*-dodecane is injected into a quiescent environment under operating conditions representative of Diesel combustion in light-duty applications. Experimental and modeling soot contributions under the Spray A configuration were reviewed by Skeen et al. [17] that compiled the results from several institutions. Among different modeling contributions, five out of six relied on the use of two-equation soot models [18–20]. In this type of models, soot production is accounted for on the basis of a phenomenological description of nucleation, surface growth, oxidation and agglomeration. In addition to an equation for soot mass fraction (Y_s), one more equation for soot number density (N_s) is solved to model surface-related phenomena.

In a broader sense, soot modeling approaches can be categorized based on the number of soot-relevant quantities to be solved: one-equation models, the aforementioned two-equation models, and detailed models. In the first group, models rely on a single equation for the amount of soot produced (Y_s) based on a simple description of soot formation and oxidation. One of the widely used one-equation models is the Hiroyasu-NSC model, which is based on the formulation proposed by Hiroyasu et al. [21] and the oxidation model by Nagle and Strickland-Constable [22]. The simplicity of the model formulation favors its use in RANS-based engine simulations over a wide range of operating conditions [23] and/or high fidelity LES-based turbulent spray flame simulations [24]. On the other side of the spectrum, detailed models not only describe the amount of soot and the number of particles produced but also account for particle size distribution. In this group, the sectional method [25–30] and the method of moments [31–34] are among the most commonly used approaches for turbulent flame applications.

In addition to the modelling results reviewed by Skeen et al. [17], results targeting the Spray A configuration by means of two-equation soot models have been reported with several type of combustion modeling approaches. These include well-mixed (WM) [35–37], conditional moment closure (CMC) [38] and transported probability density function (TPDF) [39,40] approaches. More related to the modeling methodology in this work, flamelet-based, tabulated chemistry approaches have also been used for Spray A soot modeling [27,41]. Akargun et al. [41] reported results for the flamelet generated manifold (FGM). In that work, detailed flamelet calculations were used to compute Y_s and N_s and results, neglecting turbulence and chemistry interaction (TCI), were tabulated for a single flamelet with strain rate $a = 500 \text{ 1/s}$. Aubagnac-

Karkar et al. [27] modeled soot production with a sectional model and an approximated diffusion flame (ADF) approach for several strained flamelets in conjunction with a presumed probability density function (PDF) approach to account for TCI. These flamelet-based, tabulated chemistry approaches have the advantage of reduced computational cost as chemistry is solved *a priori* and decoupled from the CFD solver.

Recently, the suitability of the flamelet/progress variable (FPV) approach for soot modeling was assessed using large-scale direct numerical simulation (DNS) data from a turbulent jet diffusion flame by Wick et al. [42]. They analyzed the uncertainty originating from the coupling of the FPV combustion model and the method of moments based detailed soot model. Errors associated with the accuracy of the rate coefficients in the *H*-abstraction- C_2H_2 -addition (HACA) mechanism were found comparable to those introduced by flamelet tabulation. It was also found that for soot processes driven by polycyclic aromatic hydrocarbon (PAH), the largest uncertainties are related to the accuracy of the chemical mechanism and the PAH-related source term in the soot model.

Set against this background, the objectives of this work are two-fold. The first objective is to extend the Unsteady Flamelet Progress Variable (UFPV) model [43–45] to include soot modeling through a two-equation soot-in-flamelet approach. The second objective is to validate the implementation under the Spray A configuration while assessing the effect of ambient gas oxygen concentration, ambient temperature and ambient mixture composition on soot production.

In Section 2, the computational setup and model formulation are presented followed by the target spray flame setup in Section 3. The validation of the UFPV model for the reference condition in terms of soot temporal evolution and soot characteristics at the quasi-steady state is reported in Section 4. Results on the effect of ambient gas oxygen concentration, temperature and composition are presented in Section 5 followed by the summary and concluding remarks in Section 6.

2 Methodology

A two-equation soot model based on the work by Vishwanathan and Reitz [20] has been implemented in the context of detailed flamelet calculations. The capabilities of the flamelet solver presented in the work by Kundu et al. [46] have been extended to account for soot production with two-way coupling between soot and the gas phase. The chemical mechanism by Narayanaswamy et al. [47] with 257 species and 1521 reactions is used to describe the

oxidation of *n*-dodecane as well as PAH chemistry needed for soot modeling. The detailed soot-in-flamelet calculations are then used within the UFPV framework, constituting a soot modeling approach in turbulent spray flames. This implementation is also an extension of the capabilities of the UFPV framework. Desantes et al. [48] demonstrated the suitability of this approach in Diesel-like spray flames by assessing the effect of the nozzle diameter on ignition and flame stabilization, while Garcia-Oliver et al. [49] extended the study to an ambient temperature sweep. The following subsections outline the computational setup and the model formulation.

2.1 Computational setup

Simulations are carried out using CONVERGE [50] CFD solver in a 102 *mm* long cylindrical domain of radius 50 *mm* that is discretized with a Cartesian mesh. Refinement is achieved through near-nozzle fixed embedding and gradient-based adaptive mesh refinement (AMR). A 10 *mm* long truncated cone of base radius 1 *mm* and top radius 5 *mm* is used for the fixed embedding. AMR is triggered based on local gradients of velocity, temperature and mixture fraction. A minimum cell size of 125 μm was chosen in AMR to better predict the liquid length based on a grid convergence study for the reference inert condition.

Turbulence is approached with the Reynolds averaged Navier-Stokes (RANS) standard $k - \varepsilon$ turbulence model accounting for round jet correction [51,52] with $C_{\varepsilon 1} = 1.55$. A Lagrangian parcel, Eulerian fluid approach is used to simulate the multi-phase flow. Table 1 shows a summary of the mesh setup and details on the turbulence model, spray model and numerical schemes [53].

Table 1. Computational setup.

CFD code	CONVERGE v2.4
Base grid size	2 <i>mm</i>
Minimum cell size through fixed embedding	0.25 <i>mm</i>
Minimum cell size through AMR	0.125 <i>mm</i>
Turbulence model	Standard $\kappa - \varepsilon$ with $C_{\varepsilon 1} = 1.55$
Breakup model	Modified Kelvin-Helmholtz Rayleigh-Taylor (KH-RT)
Droplet collision model	No time counter (NTC)
Droplet drag	Dynamic model
Evaporation	Frossling correlation

Spatial discretization	Second-order central with first-order upwind for turbulence
Time discretization	Pressure implicit with splitting of operators (PISO) algorithm
Time step	Variable time step $\sim 0.2 \mu s$

The sub-grid flame structure is modeled based on a flamelet-based manifold approach, UFPV, with TCI accounted for through presumed-PDF integration, as will be further described in Section 2.3. For comparison, results obtained using the well-mixed model are also included in the analysis for the reference condition. The WM model uses a detailed chemical kinetics solver [54] build-in within CONVERGE, where the species chemical source terms are computed at every time step for groups of computational cells (grouped in zones with bins of 5 K for temperature and 0.01 for the equivalence ratio) as a function of the mean species mass fraction and mean temperature in a given group. It is useful in the context of RANS to analyze the results from the WM model which neglects TCI in contraposition to the UFPV model which accounts for TCI.

2.2 Soot model formulation

The two-equation soot model formulation is based on the work of Vishwanathan and Reitz [20] which is an extension of the model proposed by Leung, Lindstedt and Jones [19]. In this soot model, two transport equations need to be solved in CFD according to Eq. (1).

$$\frac{DM}{Dt} = \nabla \cdot \left(\frac{\mu}{S_c} \nabla \left(\frac{M}{\rho} \right) \right) + \dot{\omega}_M, \quad (1)$$

where M is either the soot number density N_s or the soot species density ρY_s . The source term $\dot{\omega}_M$ is a combined contribution from various soot subprocesses controlling the soot mass (nucleation, surface growth and oxidation) and the number of particles (nucleation and agglomeration) produced. The specifics of the soot model implementation in the context of the UFPV model are detailed as follows.

The soot formation and oxidation mechanisms are shown in Table 2 following the same formulation in [20]. Additionally, an oxidation step through atomic oxygen (O) has been included based on the work of Guo, Liu and Smallwood [55]. Although O_2 and hydroxyl radical

(OH) remain as the major contributors to soot oxidation, O can also play a non-negligible role as reported in [56].

Table 2. Soot chemistry mechanism. Molar concentration and molar fraction of species k are denoted by $[k]$ and X_k , respectively. Reaction rate units are of $kmol/(m^3 \cdot s)$.

Step	Reaction	Reaction rate
Nucleation	$C_{16}H_{10}(A_4) \xrightarrow{\dot{\omega}_n} 16C(S) + 5H_2$	$\dot{\omega}_n = k_n[A_4]$
Surface growth	$C(S) + C_2H_2 \xrightarrow{\dot{\omega}_g} 3C(S) + H_2$	$\dot{\omega}_g = k_g[C_2H_2]$
Oxidation through O_2	$C(S) + 0.5O_2 \xrightarrow{\dot{\omega}_{O_2}} CO$	NSC model [22]
Oxidation through OH	$C(S) + OH \xrightarrow{\dot{\omega}_{OH}} CO + 0.5H_2$	$\dot{\omega}_{OH} = 0.13k_{OH}X_{OH}$
Oxidation through O	$C(S) + O \xrightarrow{\dot{\omega}_O} CO$	$\dot{\omega}_O = 0.5k_OX_O$

For the UFPV model, default values are used for nucleation [20] and oxidation through OH and O [55] while the pre-exponential factor for surface growth is reduced by a factor of six from the reference value [20], to target experimental soot volume fraction at the quasi-steady state. For the WM model, default values are used for all soot subprocesses. Finally, the net source term for the soot mass density and soot number density can be computed according to Eq. (2) and Eq. (3):

$$\dot{\omega}_{Y_s} = (16\dot{\omega}_n + 2\dot{\omega}_g - \dot{\omega}_{O_2} - \dot{\omega}_{OH} - \dot{\omega}_O)M_s, \quad (2)$$

$$\dot{\omega}_{N_s} = \dot{\omega}_{n,N_s} - \dot{\omega}_{agg}, \quad (3)$$

where $\dot{\omega}_{n,N_s}$ and $\dot{\omega}_{agg}$ accounts for the effect of nucleation and agglomeration on the number of particles produced. A more detailed description of the soot chemistry mechanism including soot reaction rate constants is reported in the Supplementary Material.

2.3 Soot-in-flamelet model approach

Detailed laminar strained flamelet calculations are carried out using an in-house solver developed at Argonne National Laboratory by Kundu et. al [46]. The use of a sparse stiff LSODES solver and an analytic Jacobian [57], which is derived *a priori*, significantly reduces the computational cost compared to a more traditional approach that uses a VODE solver [58] and a numerical Jacobian. For chemical mechanisms with less than 2000 species, such as the one used in this work, the computational cost has been shown to be proportional to the square

of the number of species when a VODE solver and a numerical Jacobian are used in contrast to the linear proportionality reported with a sparse stiff LSODES solver and an analytic Jacobian [46]. In the context of CFD simulations, the computational cost can be further reduced by decoupling chemistry integration from CFD and pre-tabulating the solutions of chemical species. In particular, chemistry is solved *a priori* based on the flamelet concept and the description of the fuel-air mixing state through mixture fraction (Z). The species net production rate $\dot{\omega}_k$ is solved for local chemical systems through ordinary differential equations. A two-way coupling is used for the interaction of the gas phase and soot production such that $\dot{\omega}_k = \dot{\omega}_k^{gas} + \dot{\omega}_k^{soot}$. Note that $\dot{\omega}_k^{soot}$ is non-zero only for the species participating in soot chemistry as shown in Table 2.

To predict soot production, the two-equation model outlined in Section 2.2 has been implemented within the flamelet solver. The flamelet equations for soot number density and soot mass fraction derived in mixture fraction space, neglecting the effect of molecular diffusion compared to thermophoretic forces, are presented in Eq. (4) and Eq. (5).

$$\begin{aligned} \rho \frac{\partial \widehat{N}_s}{\partial t} + \left[\frac{1}{4} \left(\frac{\partial \rho \chi}{\partial Z} + \frac{\chi}{D} \frac{\partial}{\partial Z} (\rho D) \right) + \frac{\chi}{2D} \rho V_s \right] \frac{\partial \widehat{N}_s}{\partial Z} \\ = (e^{-\widehat{N}_s} - 1) \left(\frac{\chi}{2D} \right)^{0.5} \frac{\partial}{\partial Z} (\rho V_s) + e^{-\widehat{N}_s} \dot{\omega}_{N_s}, \end{aligned} \quad (4)$$

$$\rho \frac{\partial Y_s}{\partial t} + \frac{1}{4} \left(\frac{\partial \rho \chi}{\partial Z} + \frac{\chi}{D} \frac{\partial}{\partial Z} (\rho D) \right) \frac{\partial Y_s}{\partial Z} = - \left(\frac{\chi}{2D} \right)^{0.5} \frac{\partial}{\partial Z} (\rho Y_s V_s) + \dot{\omega}_{Y_s}. \quad (5)$$

In Eq. (4) and Eq. (5), D accounts for diffusivity in mixture fraction space, $\widehat{N}_s = \ln(N_s + 1)$ is a change of variable needed for numerical stabilities and $V_s = -0.5(\mu/\rho T)(\chi/2D)^{0.5} \partial T/\partial Z$ is the thermophoretic velocity. Detailed derivation of the soot-in-flamelet equations, i.e., Eq. (4) and Eq. (5), and corresponding assumptions can be found in [59] and [60].

The intensity of the soot transport processes is governed by the scalar dissipation rate (χ). In order to decouple chemistry and fluid, a steady profile for χ is assumed according to Peters [61] as shown in Eq. (6).

$$\chi(a, Z) = \exp \left[-2(\operatorname{erfc}^{-1}(2Z))^2 \right] a/\pi. \quad (6)$$

The profile described by Eq. (6) is a function of the strain rate a and mixture fraction Z , but a more convenient expression, independent of the strain rate, can be derived by normalizing Eq. (6) by the scalar dissipation rate at stoichiometric conditions (χ_{st}) such that $\chi(\chi_{st}, Z) = \chi_{st} F(Z)/F(Z_{st})$.

In the context of the UFPV model, the unsteady laminar flamelet solution is re-parametrized from a temporal basis to a progress variable basis. The progress variable (Y_c) is normalized yielding to a normalized progress variable (c), $c = (Y_c - Y_c^{inert})/(Y_c^{steady} - Y_c^{inert})$, which bounds between 0 at inert state and 1 at fully burned state. The re-parametrization depends on the existence of a bijective relationship between time and the progress variable [43]. This is accomplished through a linear combination of key species mass fractions relevant to combustion and soot production, that is $Y_c = 0.75Y_{CO} + Y_{CO_2} + Y_{H_2O} + 650Y_{A4R5}$. The choice of species is based on the extensively used definition $Y_c = Y_{CO} + Y_{CO_2}$ [62–65]. The weighting factor for carbon monoxide and the inclusion of water ensure that Y_c monotonically increases with time while the inclusion of cyclopenta[cd]pyrene ($A4R5$) ensures enhanced resolution for high Y_c values at which PAH chemistry and thus soot production take place.

Turbulence-chemistry interaction is accounted for through a presumed-PDF approach assuming statistical independence between mixture fraction and the scalar dissipation rate [66]. Under the presumed-PDF approach, mean values ($\tilde{\psi}$) can be obtained according to Eq. (7).

$$\tilde{\psi}(\tilde{Z}, S, \tilde{\chi}_{st}, \tilde{t}) = \int_0^\infty \int_0^Z \psi(Z, \chi_{st}, \tilde{t}) P_Z(Z; \tilde{Z}, S) P_\chi(\chi_{st}; \tilde{\chi}_{st}, \sigma) dZ d\chi_{st}, \quad (7)$$

where $S = \tilde{Z}''^2/(\tilde{Z}(1 - \tilde{Z}))$ is a segregation factor which is a function of the mean mixture fraction (\tilde{Z}) and its variance (\tilde{Z}''^2). Mean values are then tabulated in a turbulent flamelet manifold $\tilde{\psi}(\tilde{Z}, S, \tilde{\chi}_{st}, \tilde{Y}_c)$ where $\tilde{Y}_c = \tilde{Y}_c(\tilde{Z}, S, \tilde{\chi}_{st}, \tilde{c})$. In Eq. (7), a β -PDF is used for mixture fraction in $P_Z(Z; \tilde{Z}, S)$. For the scalar dissipation rate, a log-normal function is used assuming that $\sigma = 2^{0.5}$ [43] in $P_\chi(\chi_{st}; \tilde{\chi}_{st}, \sigma)$. Mean scalar dissipation rates are computed in accordance to Eq. (8) where J is used to relate $\tilde{\chi}$ and $\tilde{\chi}_{st}$.

$$\tilde{\chi} = \left(\int_0^\infty \chi_{st} P_\chi(\chi_{st}; \tilde{\chi}_{st}, \sigma) d\chi_{st} \right) \left(F(Z_{st})^{-1} \int_0^Z F(Z) P_Z(Z; \tilde{Z}, S) dZ \right) = \tilde{\chi}_{st} J(\tilde{Z}, S). \quad (8)$$

Ultimately, the turbulent flamelet manifold is composed of lookup tables discretized with 41 points for \tilde{Z} , 17 points for S , 27 points for $\tilde{\chi}_{st}$ and 51 points for \tilde{c} . These lookup tables contain results for the mean source term of the progress variable ($\tilde{\omega}_{Y_c}$ is generic nomenclature for $\partial\tilde{Y}_c/\partial t$), mean key species mass fraction (\tilde{Y}_k), mean nucleation reaction rate ($\tilde{\omega}_n$) and mean specific reaction rates for surface soot subprocesses, namely, surface growth ($\tilde{\omega}_g^*$) and oxidation through O_2 ($\tilde{\omega}_{O_2}^*$), OH ($\tilde{\omega}_{OH}^*$) and O ($\tilde{\omega}_O^*$). The asterisk superscript is used to indicate that these soot reaction rates are specific to soot surface area (A_s) such that $\tilde{\omega}_g^* = \tilde{\omega}_g/A_s^{0.5}$, $\tilde{\omega}_{O_2}^* = \tilde{\omega}_{O_2}/A_s$, $\tilde{\omega}_{OH}^* = \tilde{\omega}_{OH}/A_s$ and $\tilde{\omega}_O^* = \tilde{\omega}_O/A_s$. Unlike gaseous species, for soot the tabulation of mean reaction rates is preferred over the tabulation of mean soot mass fraction and number density. This approach aims at avoiding the unphysical process by which soot might appear at non-existing fuel-rich conditions as reported by Carbonell, Oliva and Perez-Segarra [59]. Because the unphysical process is induced by diffusion in mixture fraction space associated with the second term on the left-hand-side of Eq. (4) and Eq. (5), Carbonell, Oliva and Perez-Segarra [59] proposed to solve the mean soot mass fraction and number density using the tabulated soot source terms.

A schematic of the coupling between the UFPV model and the main CFD code is shown in Fig. 1. The flamelet manifold is queried at runtime with mean values from the CFD solver to retrieve mean tabulated values $\tilde{\psi}(\tilde{Z}, S, \tilde{\chi}_{st}, \tilde{Y}_c)$ where $\tilde{\chi}_{st}$ is correlated to the mean scalar dissipation rate $\tilde{\chi} = C_\chi \tilde{Z}''^2 \varepsilon/k$ through the value of J as described in Eq. (8).

In terms of combustion, the coupling is achieved through the mean source term for the transport of key species computed according to Eq. (9)

$$\tilde{\omega}_k = \left(\tilde{Y}_k^{tab}(\tilde{Z}, S, \tilde{\chi}_{st}, \tilde{Y}_c(t + \Delta t)) - \tilde{Y}_k^{cell}(t) \right) / \Delta t, \quad (9)$$

where the mean progress variable at the next time step is calculated as $\tilde{Y}_c(t + \Delta t) = \tilde{Y}_c(t) + \tilde{\omega}_{Y_c}(\tilde{Z}, S, \tilde{\chi}_{st}, \tilde{Y}_c(t)) \Delta t$. Only 15 key species are transported to save computational cost. These species are $C_{12}H_{26}$, C_2H_2 , CH_2O , CO , CO_2 , H , H_2O , O , O_2 , OH , $A4$ and $A4R5$ in addition to 3 sink species (C_7H_{14} , H_2 and a virtual species $O_{2_{virt}}$) used to account for the atomic element mass (C , H and O) of the species that are not transported.

In terms of soot production, the coupling is established through the mean source terms, $\tilde{\omega}_{Y_s}$ and $\tilde{\omega}_{N_s}$, for soot species density and soot number density transport equations:

$$\tilde{\omega}_{Y_s} = (16\tilde{\omega}_n + 2\tilde{\omega}_g^* A_s^{0.5} - (\tilde{\omega}_{O_2}^* + \tilde{\omega}_{OH}^* + \tilde{\omega}_O^*) A_s) M_s, \quad (10)$$

$$\tilde{\omega}_{N_s} = \tilde{\omega}_{n,N_s} - \tilde{\omega}_{agg}. \quad (11)$$

The Supplementary Material includes the definition of the soot surface area A_s and the terms describing the contribution of nucleation ($\tilde{\omega}_{n,N_s}$) and agglomeration ($\tilde{\omega}_{agg}$) to the soot number density.

3 Target spray flame setup

Data used for model validation is from the experimental measurements in high-temperature, high-pressure vessels within the ECN [16]. Table 3 summarizes the reference fuel injection and thermodynamic conditions for Spray A, while variations in thermodynamic conditions for the assessment of the effect of ambient gas temperature and composition on soot production are reported in Table 4.

Table 3. Reference fuel injection and ambient thermodynamic conditions.

Fuel	n-dodecane
Nozzle diameter	89.4 μm
Nozzle reference number	#210675
Injection pressure	150 MPa
Fuel temperature	363 K
Ambient density	22.8 kg/m ³

The assessment of the effect of ambient conditions on soot production includes changes in ambient oxygen concentration, i.e., “13% X_{O_2} ” condition vs. “Ref $CO_2 + H_2O$ ” condition, and in ambient temperature, i.e., “Ref” condition vs. “1000 K” condition. The effect of ambient composition is also assessed by comparing the “Ref” condition and the “Ref $CO_2 + H_2O$ ” condition. As indicated by the labels, these different cases allow us to study the role that the presence of carbon dioxide (CO_2) and water (H_2O) plays on soot production. This is of particular relevance within the ECN in which two types of experimental facilities have been used. Constant-pressure vessels are operated with an ambient composition of pure oxygen (O_2)

and nitrogen (N_2) while constant-volume vessels operate with an ambient composition of O_2 , N_2 , CO_2 and H_2O . In constant-volume vessels, CO_2 and H_2O are products of a pre-burn event used to achieve the desired thermodynamic conditions for experiments. With evidence from dedicated experiments showing that the presence of CO_2 and H_2O reduces the amount of soot produced [67], it is of significant relevance to numerically investigate soot production processes with different ambient compositions.

Table 4. Ambient thermodynamic conditions for the study of the effect of ambient conditions on soot production.

Condition	Temperature	X_{O_2}	X_{N_2}	X_{CO_2}	X_{H_2O}
13% X_{O_2}	900 K	0.13	0.7709	0.0626	0.0364
Ref $CO_2 + H_2O$	900 K	0.15	0.7515	0.0622	0.0363
Ref	900 K	0.15	0.85	0	0
1000 K	1000 K	0.15	0.85	0	0

Experiments for the “13% X_{O_2} ” and “Ref $CO_2 + H_2O$ ” conditions in Table 4 were carried out in constant-volume vessel at Sandia National Laboratory [16] using nozzle #210370 (nozzle diameter of 91 μm). The experiments for the reference condition “Ref” and the high-temperature condition “1000 K” were conducted at CMT-Motores Térmicos [68] in constant-pressure vessels using nozzle #210675.

4 Analysis of the reference condition

The analysis of results throughout this section is focused on the reference condition (i.e., “Ref” in Table 4). Fuel injection and thermodynamic conditions correspond to those in Table 3. Validation results for global combustion indicators, including ignition delay (ID) and quasi-steady lift-off length (LOL), are reported in the Supplementary Material, showing a good agreement of model predictions and experimental data. As for soot, results from the two-equation soot-in-flamelet modeling approach described in Section 2 are compared to those from the WM model. In the WM model, one-way coupling between the gas phase and soot is used. Soot source terms in Eq. (1) are computed at runtime using the two-equation soot model formulation by Vishwanathan and Reitz [20].

The validation of the temporal evolution of soot is carried out in terms of its optical thickness (KL). Experimentally, KL is directly linked to the integral value of the soot volume fraction

(SVF) along the line-of-sight of the extinction path. To compare CFD results to experimental data, the mean optical thickness from the simulations was computed according to $KL = \int k_e \lambda^{-1} SVF dl$, where the incident illumination wavelength (λ) is set as 460 nm and the dimensionless extinction coefficient (k_e) is set as 7.59 in accordance to the experimental data used for validation [68]. Fig. 2 shows KL results from the experiment and the two CFD simulations. For the two CFD cases, the stoichiometric iso-contour is represented with a dashed gray line. For further validation, the spray tip penetration (defined as the axial distance to the furthest location where the mean mixture fraction reaches a value of 0.001) at each time snapshot in the temporal sequence is marked with a pink dotted line.

The sequence depicted in Fig. 2 comprises the temporal evolution of mean soot KL from its early detection (around 0.8 ms) in the experiment up to 3.6 ms after the start of injection. CFD results seem to lag in time, as at 0.8 ms there is virtually no soot formed yet in contrast to the signal recorded in the experiment. At this early time instant, $365 \mu\text{s}$ have passed since the ignition delay time in the experiment, but only $174 \mu\text{s}$ and $255 \mu\text{s}$ have passed since their respective ignition delay times for WM and UFPV results, respectively. This over-prediction in ID is in line with the delayed appearance of soot in the simulation, which is accompanied by a slightly shorter tip penetration in the subsequent time instants depicted in the figure. It has been experimentally shown that autoignition triggers an acceleration of the reacting spray [69]. The delayed autoignition in the simulation is then consistent with a delayed acceleration of the spray and a shorter spray tip penetration in comparison to the experimental observation. In terms of soot structure, the soot cloud originally forms at the fuel-rich head of the spray ($0.8\text{-}1.2 \text{ ms}$) and then evolves into a mushroom-shaped structure while mean KL peak values continue to increase. In the experiment, the head of this mushroom-shaped structure seems to be detached from the main cloud (at around 2.4 ms) and then quickly dissipated, as the main part of the reacting front runs into a quasi-steady state. As a result, the soot cloud is constituted into an ellipse-shaped structure that barely changes beyond 2.8 ms .

Qualitatively, both WM and UFPV models, reproduce the temporal evolution described for the experimental data. First, the soot cloud is seen to be formed at the fuel-rich head of the spray. Then it transitions into a mushroom-shaped structure followed by the detachment and dissipation of its head. At that point, the ellipse-shaped soot structure eventually becomes quasi-steady. This temporal evolution in the simulations is slower compared to the experiment as already indicated by the delayed appearance of the initial soot cloud. In fact, while measured KL seems to reach quasi-steady state at 2.8 ms , at 3.6 ms the predicted soot cloud is still

transitioning towards this quasi-steady state. In terms of spatial distribution, the measured KL distribution seems to fall between WM and UFPV results in the radial direction while both models over-predict the extension of the soot cloud. At 3.6 ms the WM model predicts a narrow soot structure contained within the stoichiometric surface while the UFPV model predicts a broader soot structure beyond the limit of the stoichiometric surface.

Validation of results at quasi-steady state is carried out in terms of the mean SVF field. Several mean SVF profiles are shown in Fig. 3 for the experiment, WM and UFPV models. Experimental data is obtained by deconvolution of the mean KL field averaged between 3.4 and 5.4 ms [68]. The panel to the left shows mean SVF profiles along the spray axis with the LOL location marked with vertical lines at the upper left corner. Subpanels to the right of the figure show radial profiles at several downstream locations from the nozzle exit (50 to 75 mm).

Axially, the mean SVF onset location for the WM model lags in comparison to the UFPV and experimental profiles. Considering that the ID predictions are not significantly different between WM (ID = 626.1 μs) and UFPV (ID = 545.1 μs), as reported in the Supplementary Material, the spatial shift for the WM model is mainly due to the over-prediction of LOL (LOL = 28.26 mm for the WM model vs. LOL = 17.17 mm for the UFPV model). Radially, simulation profiles are narrower (compared to the experiment) with an abrupt drop to near-zero values at around $r = 5 mm$ indicative of fast soot oxidation in the vicinity of this location. Previous studies focusing on the effect of TCI on soot predictions comparing WM and TPDF formulations [39,40] have suggested that soot radial profiles are narrower when turbulent fluctuations are not taken into account. This feature is the result of higher oxidation rates and the fact that contributions from other mixture fractions are neglected under a WM assumption for a given location in the spray [38,40]. UFPV results match the axial SVF profiles in the ramp-up region up to 55 mm in line with the good LOL agreement compared to the experimental observation. Mean SVF profiles at 50 and 55 mm from the nozzle show that UFPV results are also in good agreement with experiments in terms of radial width in the ramp-up region despite the over-prediction observed at further downstream locations. In fact, it is clear from the axial profile that both WM and UFPV models over-predict the length of the SVF structure at the quasi-steady state. It is interesting though that the decreasing slope (variable m obtained through linear fitting) in the axial profile is similar for both modeling approaches. Given the differences among the two modeling approaches in terms of sub-grid flame structure, TCI treatment and even soot model formulation, the observation of a similar decreasing slope in the mean SVF axial profile suggests that the extension of the soot structure is heavily controlled by

the mixing process and hence the air entrainment rate. The spray mixing process has been reported to be as relevant as soot kinetics in the Spray A configuration [71]. In this sense, the slightly higher slope in experiments might be indicative of a stronger entrainment process compared with simulations.

To further analyze soot spatial distribution, Fig. 4 depicts the measured and predicted mean SVF fields accompanied by the lift-off length location (vertical line), the spray radius (outermost solid line), the stoichiometric iso-contour (dashed line) and mixing trajectories (inner solid lines). The mixing trajectories are obtained by integrating the equation $dx/(u + u_{dif}) = dr/(v + v_{dif})$ where u_{dif} and v_{dif} are the diffusive components [72] of the mean velocity field induced by mixture fraction diffusion. A more detailed description of the mixing trajectory concept is reported in a previous study by the authors [48]. In Fig. 4, the starting points of references mixing trajectories, labeled as 1 and 2, are placed at 70% of the spray tip penetration in the axial direction and at 5% and 25% of the spray width in the radial direction.

Mean SVF profiles in Fig. 3 show an over-prediction of the soot structure length which is clearly seen in Fig. 4. Radial profiles also show an abrupt decrease to near-zero values around 5 mm for the WM model, a location that matches the location of the stoichiometric mixture fraction iso-surface. This abrupt decrease in the SVF radial distribution contrasts with the smoother distribution observed in the experimental data and the UFPV prediction. From Fig. 4, it is also clear that soot is mostly confined between mixing trajectories 1 and 2. The two mixing trajectories are slower, in terms of the mean residence time, compared to more radially displaced trajectories. Fig. 5 shows the integrated mean residence time that a “gas particle” would experience at each equivalence ratio traveling along mixing trajectories 1 and 2. When comparing mixing trajectories, the longer mean residence time in mixing trajectory 1 suggests that mixing trajectories closer to the axis are slower and hence more prone to produce soot. As for the investigated modeling approaches, differences between WM and UFPV results are mostly negligible for either mixing trajectory, with the exception of equivalence ratios in the vicinity of the LOL ($\tilde{\phi}$ around 2-4 or 1.5-3, depending on the trajectory). Therefore, the local mean residence time is largely independent of the TCI approach.

It is worth noting that the computational cost of running a WM simulation is in the order of 50.8×10^3 core hours while the cost of running a UFPV simulation drops down to 1.2×10^3 core hours (approximately 40 times speedup), thus confirming the expected reduced computational cost suggested in throughout Section 2.

5 Effect of ambient conditions on soot production

To study the effect of changes in ambient conditions on soot production, the analysis is focused on the effect of ambient oxygen concentration (“13% X_{O_2} ” condition vs. “Ref $CO_2 + H_2O$ ” condition), ambient CO_2 and H_2O concentration (“Ref $CO_2 + H_2O$ ” condition vs. “Ref” condition) and ambient temperature (“Ref” condition vs. “1000 K” condition). In total, four cases (including the reference condition case from Section 4) are the subject of study with the thermodynamic conditions summarized in Table 4.

The effect of the aforementioned changes in thermodynamic conditions on the flame structure at quasi-steady state is described through the analysis of the mean transverse integrated mass (TIM) results. These are obtained for a given species k by plotting $\int \tilde{Y}_k(x, r) \tilde{\rho}(x, r) 2\pi r dr$ along the axial direction. Fig. 6 show mean TIM results for formaldehyde (CH_2O), hydroxyl radical (OH) and acetylene (C_2H_2). These three species constitute a tracer for low-temperature reactions, a tracer for high-temperature reactions and crucial species for the formation and growth of PAHs [73,74], respectively. In addition to CH_2O , OH (which is scaled up by a factor of 5) and C_2H_2 , results for the soot precursor A_4 (scaled up by a factor of 150) are also included in Fig. 6.

A first noticeable feature from mean TIM results is that the peak point for CH_2O is located in the vicinity of the onset location for OH as the flame spatially transitions from the low- to the high-temperature chemistry and hence the appearance of OH comes with the consumption of CH_2O . It is also interesting to note that the LOL location is shifted upstream from the peak mean TIM for CH_2O with the change in mixture reactivity. Moreover, this change in reactivity attributed to the different evaluated ambient conditions can be inferred from the production of CH_2O and OH . The decrease in LOL goes in line with a clear drop in peak CH_2O values and a general increase of OH all over the axial direction when either ambient oxygen concentration or temperature are increased. Also, in line with the minor change in LOL comparing the “Ref $CO_2 + H_2O$ ” condition and the “Ref” condition, changes in mean TIM results are more subtle between those cases.

As for C_2H_2 and A_4 , both species are located downstream of the LOL. It is interesting to note that the peak and onset locations (onset based on a threshold of 2% of the peak value) of these species are closer to each other with the increase in ambient gas reactivity. For instance, in the low-oxygen concentration case (top panel) the onset locations for C_2H_2 and A_4 are around 20 and 31 mm, respectively, while these are around 13 and 16 mm in the high-temperature case

(bottom panel). Similarly, peak values of C_2H_2 and A_4 are located around 44 and 63 mm for the low-oxygen concentration and around 33 and 41 mm for the high-temperature case, respectively. This observation supports the choice of A_4 over C_2H_2 as soot precursor species suggested by Vishwanathan and Reitz [20] based on the experimental results in [75]. According to that, an under-estimation of soot onset location would be expected if C_2H_2 were used as soot precursor, particularly in low-reactivity conditions. With a similar flame structure, the most significant difference, among the cases studied, is the LOL location. An increase in either ambient oxygen concentration or temperature leads to a clear reduction in the LOL. In contrast, the presence of CO_2 and H_2O in the ambient gas composition produces just a minor increase compared to the case where only O_2 and N_2 ("Ref" condition) are present in the ambient gas.

To validate soot results, Fig. 7 compares the axial mean SVF profiles from a constant-volume vessel [16] (top panel), where CO_2 and H_2O in the ambient gas are produced in a pre-burn combustion, and a constant-pressure vessel [68] (bottom panel).

Results in the top panel show that the modeling approach is able to reproduce the increase in mean SVF when mean X_{O_2} goes from 13% ("13% X_{O_2} ") to 15% ("Ref $CO_2 + H_2O$ "). The good agreement in the ramp-up region, previously observed for the reference condition ("Ref" case in the bottom panel), is also seen for the two cases with CO_2 and H_2O in the ambient gas although the LOL (vertical line) is slightly over-predicted for these cases. On the contrary, sensitivity to ambient temperature is not as good, despite capturing the trend in soot production for the high-temperature condition ("1000 K" condition in the bottom panel), suggesting a low sensitivity to temperature in the soot model formulation. Previous studies also reported an insufficient dependency on ambient temperature for the Spray A configuration varying from 900 to 1000 K with a similar soot chemistry formulation to the one used in this work [38,40]. Finally, the effect of the ambient residual gas composition is seen when the "Ref $CO_2 + H_2O$ " condition in the top panel is compared with the "Ref" condition in the bottom panel. At 60 mm, the predicted mean SVF for the first case is around 5 ppm while it is slightly above 10 ppm for the second case showing an inhibiting effect of CO_2 and H_2O on soot production.

It is worth highlighting that in comparison to the "Ref" condition, the decrease in soot production with the decrease in ambient oxygen concentration or its increase due to higher ambient temperature is linked to the trend in LOL location, i.e., longer LOL for the low-oxygen concentration condition and shorter LOL for the high-temperature one. Nevertheless, the presence of CO_2 and H_2O in the ambient gas does not affect dramatically the LOL location

although a reduction in SVF is observed. These soot production trends induced by the change in ambient oxygen concentration, composition and temperature can be further explained through the analysis of key variables along the reference mixing trajectory 1 in Fig. 8.

Mean residence time results (dotted line in the bottom panel) are virtually the same for all four cases. The slightly longer mean residence time for the low-oxygen concentration case can be explained based on the state of mixing. With lower oxygen concentration, where the mean mixture fraction distribution is essentially the same but mean equivalence ratio values shift away from the nozzle orifice, it takes longer for a “gas particle” on the mixing trajectory to reach the same mean equivalence ratio compared to any of the cases with higher oxygen concentration. Similarly, mean temperature results (solid line in the bottom panel) show just small variations with the change in ambient oxygen concentration and composition while the increase in ambient temperature induces a richer onset mean equivalence ratio consistent with shorter LOL and increased mixture reactivity for this condition.

In terms of mean species mass fractions (middle panel), enhanced ambient gas reactivity with higher mean X_{O_2} comes with increased production of both C_2H_2 and A_4 . That is not the case when the ambient gas composition is changed. The “Ref” and “Ref $CO_2 + H_2O$ ” conditions show similar C_2H_2 profiles while the mean mass fraction of the soot precursor is clearly lower for the latter case pointing at a strong effect of CO_2 and H_2O on the PAH species but not on C_2H_2 . Differences in mean mass fraction of the soot surface growth and precursor species are also crucial in the high-temperature case in which the onset point (based on a threshold of 2% of the peak value) takes place at mean equivalence ratios as rich as $\tilde{\phi} = 4.9$ for C_2H_2 and $\tilde{\phi} = 4$ for A_4 while the reference condition shows leaner onset mixtures (around $\tilde{\phi} = 3.9$ and $\tilde{\phi} = 3.3$ for C_2H_2 and A_4 , respectively) as well as lower peak values consistent with decreased soot production. Lastly, mean soot mass fraction results (solid line in the top panel) confirm the trend already seen for mean SVF along the spray axis. Moreover, the increase in soot production with any of the ambient gas variations is accompanied by an increase in mean soot particle diameter (dotted line in the top panel).

In summary, taking into account that there are virtually no changes in the residence time results, it is clear that soot production trends in this study are the result of changes in the spray mixture reactivity, meaning that the onset mean equivalence ratio at which the high-temperature region appears and the concentration of soot precursor and surface growth species are the most relevant variables.

6 Summary and conclusions

A two-equation soot-in-flamelet modeling approach has been applied to the study of soot production under Spray A conditions. The two-equation soot model used in this work has been implemented in the context of detailed flamelet calculations with two-way coupling between the gas phase and soot. Laminar flamelet results were integrated with a presumed-PDF approach to account for TCI and then tabulated in a turbulent flamelet manifold that was later used in the UFPV model. Tabulated soot source terms were used in soot transport equations within CFD simulations. Various Spray A thermodynamic conditions were simulated to assess the effect of ambient gas conditions on soot production. For the reference condition, a WM modeling approach was further used for comparison.

Key findings are summarized as follows:

- Both UFPV and WM models reproduce soot temporal evolution that is characterized by an initial mushroom-shaped soot structure in the fuel-rich head of the spray and its transition into an ellipse-shaped structure at quasi-steady state. Soot temporal evolution has been shown to be slower in simulations compared to experimental KL measurements. At the quasi-steady state, UFPV results show good quantitative agreement in the ramp-up region in the axial and radial mean SVF profiles. In the region further downstream, both WM and UFPV modeling approaches over-predict the extension of the mean SVF structure. A similar decreasing slope in the mean SVF profile along the spray axis suggests that the length of the soot structure is mainly controlled by the rate of mixing. Lastly, the computational cost was reduced by a factor of around 40 using the developed UFPV model compared with the WM model.
- The production of soot is favored along mixing trajectories close to the spray axis. Residence times along these mixing trajectories are higher compared to those in radially displaced locations. Moreover, in the $\tilde{\phi} - \tilde{T}$ coordinate, mixing trajectories enclosing most of the soot structure are confined in a narrow band of high-temperature, rich-fuel mixtures. From a combustion point of view, soot is observed to be a slow species that is mainly found at \tilde{c} levels above 0.9.
- Variations in ambient oxygen concentration, composition and temperature show that, with virtually the same mean residence time, the high-temperature mean equivalence ratio onset and concentrations of A_4 and C_2H_2 are the key variables controlling soot production. Increasing ambient oxygen concentration or temperature promotes the

combustion of richer mixtures and results in higher concentrations of soot-related key species. The presence of CO_2 and H_2O as part of the ambient gas lowers the concentration of A_4 and consequently soot production rate. CFD results were validated against SVF measurements with good quantitative agreement in the ramp-up region with the exception of the high-temperature case for which the soot model does not seem to be sensitive enough to temperature.

Acknowledgements

This work was partially funded by the Government of Spain through the CHEST Project (TRA2017-89139-C2-1-R) and by Universitat Politècnica de València through Programa de Ayudas de Investigación y Desarrollo (PAID-01-16) and Ayudas para movilidad dentro del Programa para la Formación de Personal investigador 2017. We gratefully acknowledge the computing resources provided on Bebop, a computing cluster operated by the Laboratory Computing Resource Center at Argonne National Laboratory. The technical support of Convergent Science is also greatly acknowledged.

Disclaimer

The submitted manuscript has been created by UChicago Argonne, LLC, Operator of Argonne National Laboratory (Argonne). Argonne, a U.S. Department of Energy Office of Science laboratory, is operated under Contract No. DE-AC02-06CH11357. The U.S. Government retains for itself, and others acting on its behalf, a paid-up nonexclusive, irrevocable worldwide license in said article to reproduce, prepare derivative works, distribute copies to the public, and perform publicly and display publicly, by or on behalf of the Government. This research was funded by U.S. DOE Office of Vehicle Technologies, Office of Energy Efficiency and Renewable Energy under Contract No. DE-AC02-06CH11357.

References

- [1] P.K. Senecal, F. Leach, Diversity in transportation: Why a mix of propulsion technologies is the way forward for the future fleet, *Results Eng.* 4 (2019) 100060. <https://doi.org/10.1016/j.rineng.2019.100060>.
- [2] J.R. Serrano, R. Novella, P. Piqueras, Why the Development of Internal Combustion Engines Is Still Necessary to Fight against Global Climate Change from the Perspective of Transportation, *Appl. Sci.* 9 (2019) 4597. <https://doi.org/10.3390/app9214597>.

- [3] M.M. Thackeray, C. Wolverton, E.D. Isaacs, Electrical energy storage for transportation—approaching the limits of, and going beyond, lithium-ion batteries, *Energy Environ. Sci.* 5 (2012) 7854. <https://doi.org/10.1039/c2ee21892e>.
- [4] M.O. Andreae, C.D. Jones, P.M. Cox, Strong present-day aerosol cooling implies a hot future, *Nature*. 435 (2005) 1187–1190. <https://doi.org/10.1038/nature03671>.
- [5] M.O. Andreae, D. Rosenfeld, Aerosol–cloud–precipitation interactions. Part 1. The nature and sources of cloud-active aerosols, *Earth-Sci. Rev.* 89 (2008) 13–41. <https://doi.org/10.1016/j.earscirev.2008.03.001>.
- [6] M.Z. Jacobson, Short-term effects of controlling fossil-fuel soot, biofuel soot and gases, and methane on climate, Arctic ice, and air pollution health, *J. Geophys. Res.* 115 (2010). <https://doi.org/10.1029/2009JD013795>.
- [7] J. Hansen, L. Nazarenko, Soot climate forcing via snow and ice albedos, *Proc. Natl. Acad. Sci.* 101 (2004) 423–428. <https://doi.org/10.1073/pnas.2237157100>.
- [8] O.L. Hadley, T.W. Kirchstetter, Black-carbon reduction of snow albedo, *Nat. Clim. Change*. 2 (2012) 437–440. <https://doi.org/10.1038/nclimate1433>.
- [9] I.M. Kennedy, The health effects of combustion-generated aerosols, *Proc. Combust. Inst.* 31 (2007) 2757–2770. <https://doi.org/10.1016/j.proci.2006.08.116>.
- [10] K.S. Hougaard, K.A. Jensen, P. Nordly, C. Taxvig, U. Vogel, A.T. Saber, H. Wallin, Effects of prenatal exposure to diesel exhaust particles on postnatal development, behavior, genotoxicity and inflammation in mice, *Part. Fibre Toxicol.* 5 (2008) 3. <https://doi.org/10.1186/1743-8977-5-3>.
- [11] I.N. Krivoshto, J.R. Richards, T.E. Albertson, R.W. Derlet, The Toxicity of Diesel Exhaust: Implications for Primary Care, *J. Am. Board Fam. Med.* 21 (2008) 55–62. <https://doi.org/10.3122/jabfm.2008.01.070139>.
- [12] M. Shiraiwa, K. Selzle, U. Pöschl, Hazardous components and health effects of atmospheric aerosol particles: reactive oxygen species, soot, polycyclic aromatic compounds and allergenic proteins, *Free Radic. Res.* 46 (2012) 927–939. <https://doi.org/10.3109/10715762.2012.663084>.
- [13] Regulation (EC) No 764/2008 of the European Parliament and of the Council, 2015. https://doi.org/10.1007/978-1-137-54482-7_19.

- [14] R.S.G. Baert, P.J.M. Frijters, B. Somers, C.C.M. Luijten, W. de Boer, Design and Operation of a High Pressure, High Temperature Cell for HD Diesel Spray Diagnostics: Guidelines and Results, in: 2009. <https://doi.org/10.4271/2009-01-0649>.
- [15] L.M. Pickett, C.L. Genzale, G. Bruneaux, L.-M. Malbec, L. Hermant, C. Christiansen, J. Schramm, Comparison of Diesel Spray Combustion in Different High-Temperature, High-Pressure Facilities, *SAE Int. J. Engines*. 3 (2010) 156–181.
- [16] Engine Combustion Network, (2020). <https://ecn.sandia.gov/>.
- [17] S.A. Skeen, J. Manin, L.M. Pickett, E. Cenker, G. Bruneaux, K. Kondo, T. Aizawa, F. Westlye, K. Dalen, A. Ivarsson, T. Xuan, J.M. Garcia-Oliver, Y. Pei, S. Som, W. Hu, R.D. Reitz, T. Lucchini, G. D'Errico, D. Farrace, S.S. Pandurangi, Y.M. Wright, M.A. Chishty, M. Bolla, E. Hawkes, A Progress Review on Soot Experiments and Modeling in the Engine Combustion Network (ECN), *SAE Int. J. Engines*. 9 (2016) 883–898. <https://doi.org/10.4271/2016-01-0734>.
- [18] J.B. Moss, C.D. Stewart, K.J. Syed, Flowfield modelling of soot formation at elevated pressure, *Symp. Int. Combust.* 22 (1989) 413–423. [https://doi.org/10.1016/S0082-0784\(89\)80048-7](https://doi.org/10.1016/S0082-0784(89)80048-7).
- [19] K.M. Leung, R.P. Lindstedt, W.P. Jones, A simplified reaction mechanism for soot formation in nonpremixed flames, *Combust. Flame*. 87 (1991) 289–305. [https://doi.org/10.1016/0010-2180\(91\)90114-Q](https://doi.org/10.1016/0010-2180(91)90114-Q).
- [20] G. Vishwanathan, R.D. Reitz, Development of a Practical Soot Modeling Approach and Its Application to Low-Temperature Diesel Combustion, *Combust. Sci. Technol.* 182 (2010) 1050–1082. <https://doi.org/10.1080/00102200903548124>.
- [21] H. Hiroyasu, T. Kadota, Models for combustion and formation of nitric oxide and soot in direct injection diesel engines, *SAE Trans.* (1976) 513–526.
- [22] J. Nagle, R.F. Strickland-Constable, Oxidation of carbon between 1000-2000°C, in: *Proc. Fifth Carbon Conf.*, Pergamon Press, London, 1962: p. 154.
- [23] A.B. Dempsey, P. Seiler, K. Svensson, Y. Qi, A Comprehensive Evaluation of Diesel Engine CFD Modeling Predictions Using a Semi-Empirical Soot Model over a Broad Range of Combustion Systems, *SAE Int. J. Engines*. 11 (2018). <https://doi.org/10.4271/2018-01-0242>.
- [24] A.A. Moiz, M.M. Ameen, S.-Y. Lee, S. Som, Study of soot production for double

injections of n-dodecane in CI engine-like conditions, *Combust. Flame*. 173 (2016) 123–131. <https://doi.org/10.1016/j.combustflame.2016.08.005>.

[25] P. Rodrigues, B. Franzelli, R. Vicquelin, O. Gicquel, N. Darabiha, Coupling an LES approach and a soot sectional model for the study of sooting turbulent non-premixed flames, *Combust. Flame*. 190 (2018) 477–499. <https://doi.org/10.1016/j.combustflame.2017.12.009>.

[26] S. Gkantonas, M. Sirignano, A. Giusti, A. D'Anna, E. Mastorakos, COMPREHENSIVE SOOT PARTICLE SIZE DISTRIBUTION MODELLING OF A MODEL RICH-QUENCH-LEAN BURNER, in: 11th Mediterr. Combust. Symp., Tenerife Spain, 2019.

[27] D. Aubagnac-Karkar, J.-B. Michel, O. Colin, N. Darabiha, Combustion and soot modelling of a high-pressure and high-temperature Dodecane spray, *Int. J. Engine Res*. 19 (2018) 434–448. <https://doi.org/10.1177/1468087417714351>.

[28] D. Aubagnac-Karkar, J.-B. Michel, O. Colin, P.E. Vervisch-Kljakic, N. Darabiha, Sectional soot model coupled to tabulated chemistry for Diesel RANS simulations, *Combust. Flame*. 162 (2015) 3081–3099. <https://doi.org/10.1016/j.combustflame.2015.03.005>.

[29] P.P. Duvvuri, S. Sukumaran, R.K. Shrivastava, S. Sreedhara, Modeling soot particle size distribution in diesel engines, *Fuel*. 243 (2019) 70–78. <https://doi.org/10.1016/j.fuel.2019.01.104>.

[30] F. Ibrahim, W.M.F. Wan Mahmood, S. Abdullah, M.R.A. Mansor, Comparison of Simple and Detailed Soot Models in the Study of Soot Formation in a Compression Ignition Diesel Engine, in: 2017. <https://doi.org/10.4271/2017-01-1006>.

[31] F. Bisetti, G. Blanquart, M.E. Mueller, H. Pitsch, On the formation and early evolution of soot in turbulent nonpremixed flames, *Combust. Flame*. 159 (2012) 317–335. <https://doi.org/10.1016/j.combustflame.2011.05.021>.

[32] P. Donde, V. Raman, M.E. Mueller, H. Pitsch, LES/PDF based modeling of soot–turbulence interactions in turbulent flames, *Proc. Combust. Inst*. 34 (2013) 1183–1192. <https://doi.org/10.1016/j.proci.2012.07.055>.

[33] A. Hatzipanagiotou, P. Wenzel, C. Krueger, R. Payri, J.M. Garcia-Oliver, W. Vera-Tudela, T. Koch, Soot Model Calibration Based on Laser Extinction Measurements, in: 2016. <https://doi.org/10.4271/2016-01-0590>.

[34] K.M. Mukut, S.P. Roy, Effect of O₂ concentration in ambient mixture and multiphase

radiation on pollutant formation in ECN spray-A, *Combust. Theory Model.* 24 (2020) 549–572. <https://doi.org/10.1080/13647830.2020.1721561>.

[35] H. Wang, Y. Ra, M. Jia, R.D. Reitz, Development of a reduced n -dodecane-PAH mechanism and its application for n -dodecane soot predictions, *Fuel.* 136 (2014) 25–36. <https://doi.org/10.1016/j.fuel.2014.07.028>.

[36] K.M. Pang, M. Jangi, X.-S. Bai, J. Schramm, Evaluation and optimisation of phenomenological multi-step soot model for spray combustion under diesel engine-like operating conditions, *Combust. Theory Model.* 19 (2015) 279–308. <https://doi.org/10.1080/13647830.2015.1019929>.

[37] M.F.A. Razak, F. Salehi, M.A. Chishty, An Analysis of Turbulent Mixing Effects on the Soot Formation in High Pressure n-dodecane Sprays, *Flow Turbul. Combust.* 103 (2019) 605–624. <https://doi.org/10.1007/s10494-019-00045-9>.

[38] S.S. Pandurangi, M. Bolla, Y.M. Wright, K. Boulouchos, S.A. Skeen, J. Manin, L.M. Pickett, Onset and progression of soot in high-pressure n-dodecane sprays under diesel engine conditions, *Int. J. Engine Res.* 18 (2017) 436–452. <https://doi.org/10.1177/1468087416661041>.

[39] M. Bolla, M.A. Chishty, E.R. Hawkes, Q.N. Chan, S. Kook, Influence of turbulent fluctuations on radiation heat transfer, NO and soot formation under ECN Spray A conditions, *Proc. Combust. Inst.* 36 (2017) 3551–3558. <https://doi.org/10.1016/j.proci.2016.06.173>.

[40] M.A. Chishty, M. Bolla, E.R. Hawkes, Y. Pei, S. Kook, Soot formation modelling for n-dodecane sprays using the transported PDF model, *Combust. Flame.* 192 (2018) 101–119. <https://doi.org/10.1016/j.combustflame.2018.01.028>.

[41] H. Yigit Akargun, B. Akkurt, N. G. Deen, L.M.T. Somers, Extending the Flamelet Generated Manifold for Soot and NO_x Modeling in Diesel Spray Combustion, *Proc. Int. Symp. Diagn. Model. Combust. Intern. Combust. Engines.* 2017.9 (2017) A105. <https://doi.org/10.1299/jmsesdm.2017.9.A105>.

[42] A. Wick, A. Attili, F. Bisetti, H. Pitsch, DNS-driven analysis of the Flamelet/Progress Variable model assumptions on soot inception, growth, and oxidation in turbulent flames, *Combust. Flame.* 214 (2020) 437–449. <https://doi.org/10.1016/j.combustflame.2020.01.012>.

[43] B. Naud, R. Novella, J.M. Pastor, J.F. Winklinger, RANS modelling of a lifted H₂/N₂ flame using an unsteady flamelet progress variable approach with presumed PDF, *Combust.*

Flame. 162 (2015) 893–906. <https://doi.org/10.1016/j.combustflame.2014.09.014>.

[44] J.M. Desantes, J.M. García-Oliver, R. Novella, E.J. Pérez-Sánchez, Application of an unsteady flamelet model in a RANS framework for spray A simulation, *Appl. Therm. Eng.* 117 (2017) 50–64. <https://doi.org/10.1016/j.applthermaleng.2017.01.101>.

[45] F. Payri, J.M. García-Oliver, R. Novella, E.J. Pérez-Sánchez, Influence of the n-dodecane chemical mechanism on the CFD modelling of the diesel-like ECN Spray A flame structure at different ambient conditions, *Combust. Flame.* 208 (2019) 198–218. <https://doi.org/10.1016/j.combustflame.2019.06.032>.

[46] P. Kundu, M.M. Ameen, C. Xu, U. Unnikrishnan, T. Lu, S. Som, Implementation of Detailed Chemistry Mechanisms in Engine Simulations, *J. Eng. Gas Turbines Power.* 141 (2018). <https://doi.org/10.1115/1.4041281>.

[47] K. Narayanaswamy, P. Pepiot, H. Pitsch, A chemical mechanism for low to high temperature oxidation of n-dodecane as a component of transportation fuel surrogates, *Combust. Flame.* 161 (2014) 866–884. <https://doi.org/10.1016/j.combustflame.2013.10.012>.

[48] J.M. Desantes, J.M. Garcia-Oliver, R. Novella, L. Pachano, A numerical study of the effect of nozzle diameter on diesel combustion ignition and flame stabilization, *Int. J. Engine Res.* 21 (2020) 101–121. <https://doi.org/10.1177/1468087419864203>.

[49] J.M. García-Oliver, R. Novella, J.M. Pastor, L. Pachano, Computational study of ECN Spray A and Spray D combustion at different ambient temperature conditions, *Transp. Eng.* 2 (2020) 100027. <https://doi.org/10.1016/j.treng.2020.100027>.

[50] CONVERGE CFD Software, (n.d.). <https://convergecf.com>.

[51] S.B. POPE, An explanation of the turbulent round-jet/plane-jet anomaly, *AIAA J.* 16 (1978) 279–281. <https://doi.org/10.2514/3.7521>.

[52] R. Novella, A. García, J.M. Pastor, V. Domenech, The role of detailed chemical kinetics on CFD diesel spray ignition and combustion modelling, *Math. Comput. Model.* 54 (2011) 1706–1719. <https://doi.org/10.1016/j.mcm.2010.12.048>.

[53] CONVERGE Manual, Convergent Science, 2016.

[54] P.K. Senecal, E. Pomraning, K.J. Richards, T.E. Briggs, C.Y. Choi, R.M. McDavid, M.A. Patterson, Multi-Dimensional Modeling of Direct-Injection Diesel Spray Liquid Length

and Flam Lift-off Length using CFD an Parallel Detailed Chemistry, in: SAE Tech. Pap., 2003: pp. 1331–1351.

[55] H. Guo, F. Liu, G.J. Smallwood, Soot and NO formation in counterflow ethylene/oxygen/nitrogen diffusion flames, *Combust. Theory Model.* 8 (2004) 475–489. <https://doi.org/10.1088/1364-7830/8/3/003>.

[56] M. Frenklach, Z. Liu, R.I. Singh, G.R. Galimova, V.N. Azyazov, A.M. Mebel, Detailed, sterically-resolved modeling of soot oxidation: Role of O atoms, interplay with particle nanostructure, and emergence of inner particle burning, *Combust. Flame.* 188 (2018) 284–306. <https://doi.org/10.1016/j.combustflame.2017.10.012>.

[57] C. Xu, Y. Gao, Z. Ren, T. Lu, A sparse stiff chemistry solver based on dynamic adaptive integration for efficient combustion simulations, *Combust. Flame.* 172 (2016) 183–193. <https://doi.org/10.1016/j.combustflame.2016.07.009>.

[58] P.N. Brown, G.D. Byrne, A.C. Hindmarsh, VODE: A Variable-Coefficient ODE Solver, *SIAM J. Sci. Stat. Comput.* 10 (1989) 1038–1051. <https://doi.org/10.1137/0910062>.

[59] D. Carbonell, A. Oliva, C.D. Perez-Segarra, Implementation of two-equation soot flamelet models for laminar diffusion flames, *Combust. Flame.* 156 (2009) 621–632. <https://doi.org/10.1016/j.combustflame.2008.12.003>.

[60] D. Carbonell Sánchez, Numerical studies of diffusion flames. Special emphasis on flamelet concept and soot formation, PhD Thesis, Universitat Politècnica de Catalunya, 2008.

[61] N. Peters, *Turbulent Combustion*, Cambridge University Press, Cambridge, 2000. <https://doi.org/10.1017/CBO9780511612701>.

[62] E. Perez, Application of a flamelet-based combustion model to diesel-like reacting sprays, Universitat Politècnica de València, 2019.

[63] L.-H. Dorey, N. Bertier, L. Tessé, F. Dupoirieux, Soot and radiation modeling in laminar ethylene flames with tabulated detailed chemistry, *Comptes Rendus Mécanique.* 339 (2011) 756–769. <https://doi.org/10.1016/j.crme.2011.09.004>.

[64] J.F. Winklinger, Implementation of a Combustion Model based on the Flamelet Concept and its Application to turbulent reactive Sprays, Universitat Politècnica de València, 2014.

[65] B. Fiorina, O. Gicquel, L. Vervisch, S. Carpentier, N. Darabiha, Approximating the

chemical structure of partially premixed and diffusion counterflow flames using FPI flamelet tabulation, *Combust. Flame.* 140 (2005) 147–160. <https://doi.org/10.1016/j.combustflame.2004.11.002>.

[66] T. Poinso, D. Veynante, *Theoretical and numerical combustion*, RT Edwards, Inc., 2005.

[67] C. Patel, C. Hespel, T.L. Nguyen, F. Foucher, C. Mounaïm-Rousselle, Effect of exhaust gas recirculation composition on soot in ECN spray A conditions, *Oil Gas Sci. Technol. – Rev. D’IFP Energ. Nouv.* 75 (2020) 34. <https://doi.org/10.2516/ogst/2020028>.

[68] T. Xuan, J.M. Desantes, J.V. Pastor, J.M. Garcia-Oliver, Soot temperature characterization of spray a flames by combined extinction and radiation methodology, *Combust. Flame.* 204 (2019) 290–303. <https://doi.org/10.1016/j.combustflame.2019.03.023>.

[69] R. Payri, J.M. García-Oliver, T. Xuan, M. Bardi, A study on diesel spray tip penetration and radial expansion under reacting conditions, *Appl. Therm. Eng.* 90 (2015) 619–629. <https://doi.org/10.1016/j.applthermaleng.2015.07.042>.

[70] J. Benajes, R. Payri, M. Bardi, P. Martí-Aldaraví, Experimental characterization of diesel ignition and lift-off length using a single-hole ECN injector, *Appl. Therm. Eng.* 58 (2013) 554–563. <https://doi.org/10.1016/j.applthermaleng.2013.04.044>.

[71] S.F. Fernandez, C. Paul, A. Sircar, A. Imren, D.C. Haworth, S. Roy, M.F. Modest, Soot and spectral radiation modeling for high-pressure turbulent spray flames, *Combust. Flame.* 190 (2018) 402–415. <https://doi.org/10.1016/j.combustflame.2017.12.016>.

[72] K. Kuo, *Principles of Combustion*, John Wiley & Sons, Inc, New York, 1986.

[73] Bockhorn, *Soot Formation in Combustion. Mechanisms and Models*, Springer- Verlag, Berlin Heidelberg, 1994.

[74] J. Warnatz, U. Maas, R.W. Dibble, *Combustion*, Springer, Berlin, 2006.

[75] T. Aizawa, H. Kosaka, Investigation of early soot formation process in a diesel spray flame via excitation—emission matrix using a multi-wavelength laser source, *Int. J. Engine Res.* 9 (2008) 79–97. <https://doi.org/10.1243/14680874JER01407>.

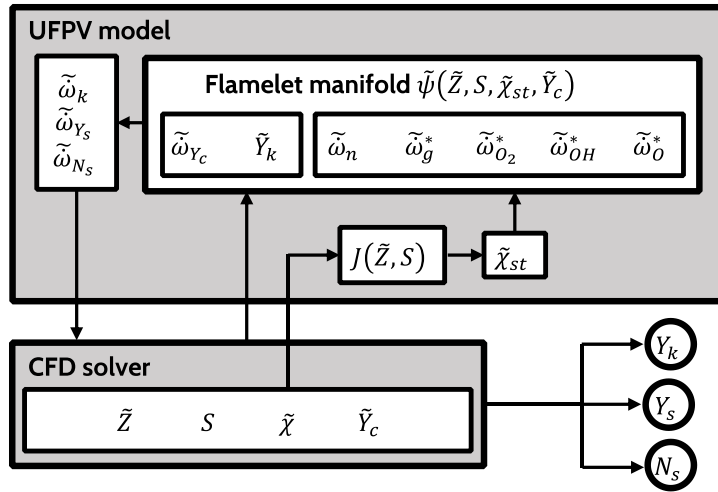


Fig. 1. Schematic of the coupling between the UFPV model and the CFD code.

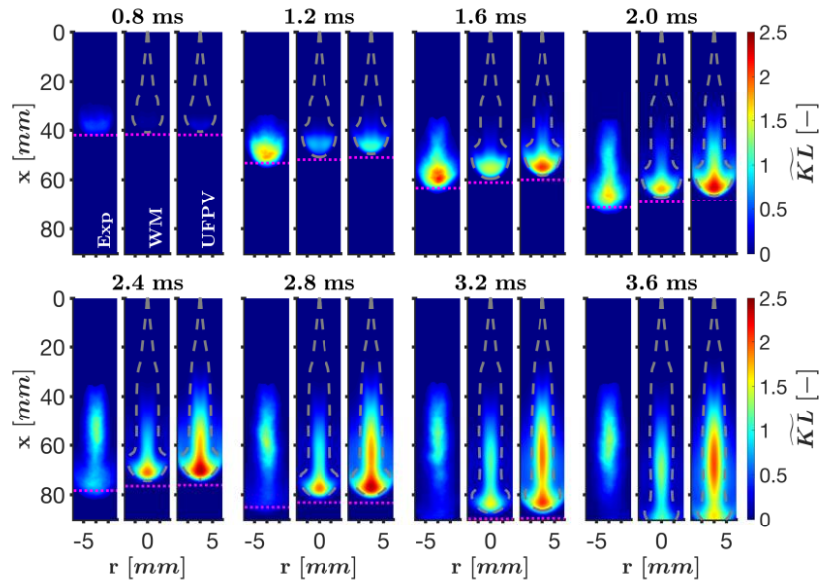


Fig. 2. Soot optical thickness temporal evolution for the experiment, WM and UFPV models. Stoichiometric iso-contour and spray tip penetration are included with a gray dashed line and a pink dotted line, respectively. Experimental data is from [68].

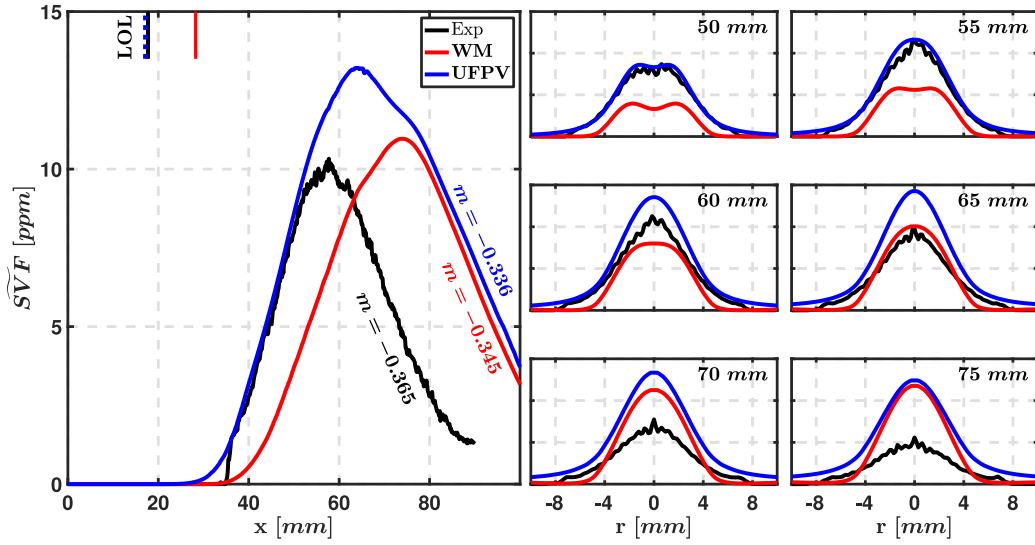


Fig. 3. Mean soot volume fraction axial and radial profiles at quasi-steady state for the experiment, WM and UFPV models. Vertical lines in the upper left corner mark the lift-off length location. Radial profile locations from the nozzle are included in the subpanels upper right corner. Experimental soot data from [68] and lift-off length data from [70].

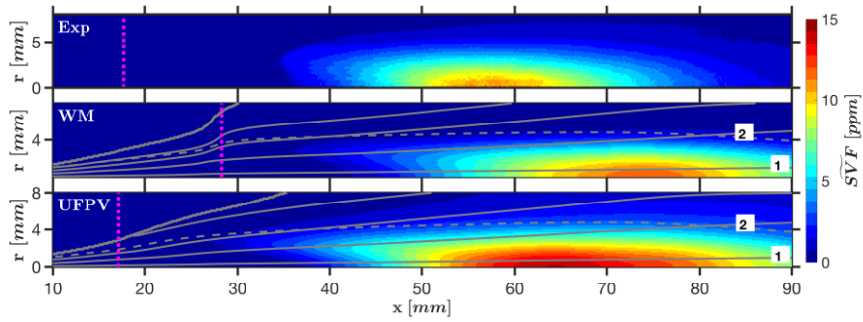


Fig. 4. Mean soot volume fraction field at quasi-steady state for the experiment (top), WM model (middle) and UFPV model (bottom). Vertical dotted line marks the LOL location. For simulation results, the spray radius, mixing trajectories and the stoichiometric iso-contour are also included. Experimental data from [68].

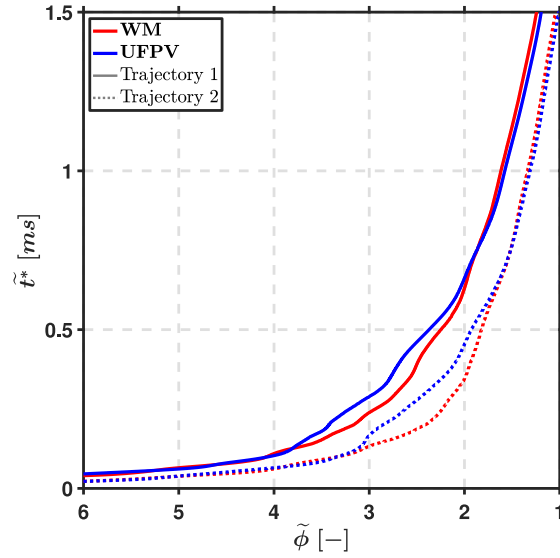


Fig. 5. Mean residence time for the WM and UFPV models integrated over reference mixing trajectory 1 (solid lines) and 2 (dotted lines).

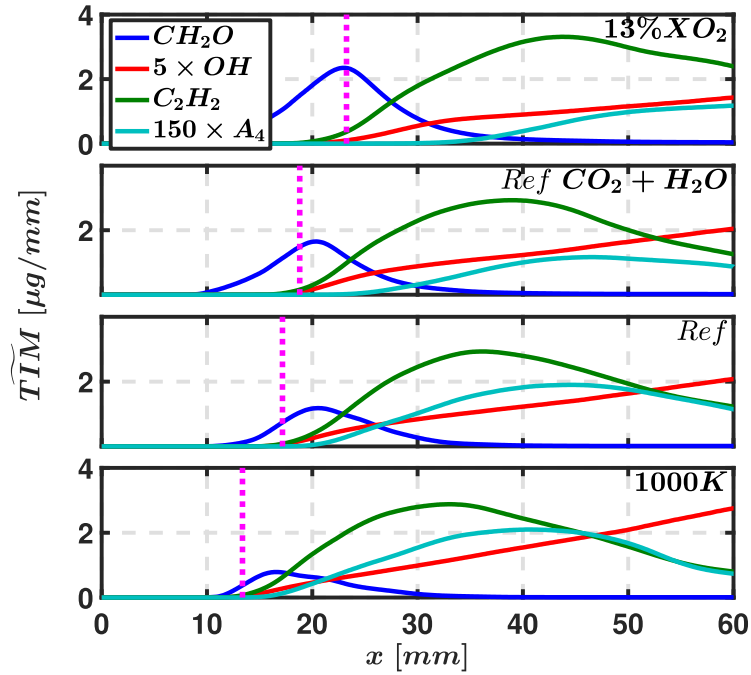


Fig. 6. Effect of ambient conditions on CH_2O , OH , C_2H_2 and A_4 mean transverse integrated mass. A vertical dotted line marks the LOL location.

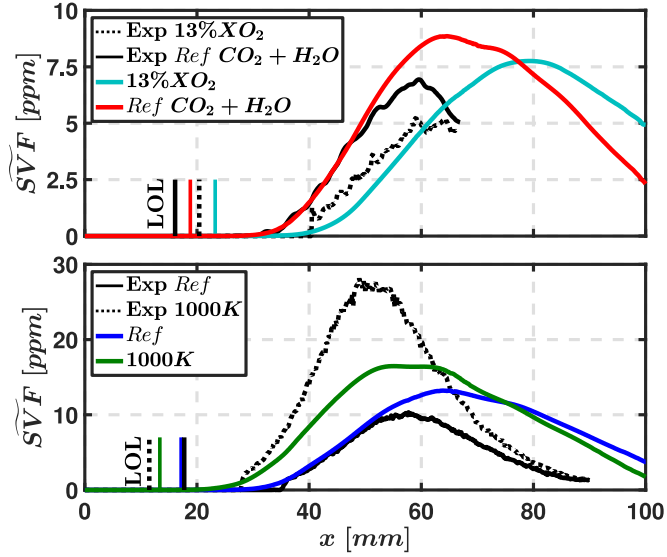


Fig. 7. Mean soot volume fraction axial profile at quasi-steady state. Top panel: effect of ambient oxygen concentration. Bottom panel: effect of ambient temperature. Lift-off length location marked with a vertical line in both panels. Experimental data from [16] (top panel) and [68,70] (bottom panel).

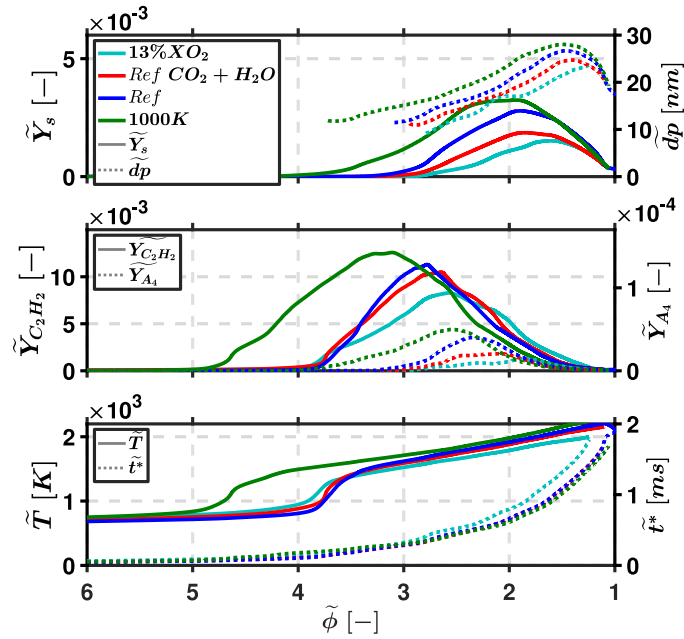


Fig. 8. Effect of ambient conditions on soot production key variables along reference mixing trajectory 1. Top panel: mean soot mass fraction (solid line) and mean soot particle diameter (dotted line). Middle panel: C_2H_2 (solid line) and A_4 (dotted line) mean mass fraction. Bottom panel: mean temperature (solid line) and mean residence time (dotted line).